Ferromagnetic moment in the magnetoelectric antiferromagnet $Co_4Ta_2O_9$: Evidence of the $P1$ magnetic space group

Rahul Goel,[1,2,3] Kwanghyo Son,[4,5] Matthias J. Gutmann,[6] Dong Gun Oh,[7] Kapil Kumar,[3] Anzar Ali,[1,2,8] Suk Jin Mun,[1,2] Dnyaneshwar Bhosale,[1,2,*] Gideok Kim,[1,8,9] Nara Lee,[7] Young Jai Choi,[7] Sang-Wook Cheong,[10,11] Valery Kiryukhin,[10] and Sungkyun Choi[1,2,3,10,†]

[1]*Center for Integrated Nanostructure Physics, Institute for Basic Science (IBS), Suwon 16419, Republic of Korea*
[2]*Sungkyunkwan University, Suwon 16419, Republic of Korea*
[3]*Center for Van der Waals Quantum Solids, Institute for Basic Science (IBS), Pohang 37673, Republic of Korea*
[4]*Max Planck Institute for Intelligent Systems, Heisenbergstrasse 3, 70569 Stuttgart, Germany*
[5]*Department of Physics Education, Kongju National University, Gongju 32588, Republic of Korea*
[6]*ISIS Facility, Rutherford Appleton Laboratory, Chilton, Didcot OX11 0QX, United Kingdom*
[7]*Department of Physics, Yonsei University, Seoul 03722, Republic of Korea*
[8]*Max Planck Institute for Solid State Research, Heisenbergstrasse 1, 70569 Stuttgart, Germany*
[9]*Department of Energy Science, Sungkyunkwan University, Suwon 16419, Republic of Korea*
[10]*Department of Physics and Astronomy, Rutgers University, Piscataway, New Jersey 08854, USA*
[11]*Keck Center for Quantum Magnetism, Rutgers University, Piscataway, New Jersey 08854, USA*

(Received 10 March 2025; accepted 22 October 2025; published 20 November 2025)

Exploring ferromagnetic moments in magnetoelectric materials is of both fundamental and technological importance. It enables the control of the correlated state using an uncompensated moment. However, its material realization is challenging owing to its exclusive microscopic mechanisms. Here, we report a nearly isotropic ferromagnetic moment in the magnetoelectric antiferromagnet $Co_4Ta_2O_9$, by performing dc and ac magnetic susceptibility, magnetization, and neutron diffraction measurements on identical single crystals. Combined with the group theory analysis, we demonstrate a $P1$ magnetic space group. This implies that physical activities can occur along any crystallographic direction, which explains the unusual magnetoelectric property of $Co_4Ta_2O_9$. The ground state is classified as the M-type altermagnet based on the magnetic point group. Our study provides essential information to resolve the debate on the magnetic ground state and understand the magnetoelectric properties of the related compound with the prospect of observing and examining the $P1$ magnetic space group or ferromagnet in ferroelectrics.

DOI: 10.1103/7gx9-wx2b

I. INTRODUCTION

Magnetoelectric (ME) and multiferroic materials [1,2] provide excellent opportunities to utilize the crossed coupling between electric polarization and magnetic moment. Multifunctional applications can be designed using this coupling by manipulating the magnetic (electronic) state with an external electric (magnetic) field. Thus, various forms of magnetoelectric compounds have been examined, ranging from three-dimensional [3] and two-dimensional van der Waals materials [4] to thin films [5].

Most magnetoelectric compounds are ferroelectric and antiferromagnetic, where magnetic moments are canceled in typical collinear antiferromagnetic structures. Thus, they do not have uncompensated magnetic moments. This is disadvantageous because the presence of a ferromagnetic moment in magnetoelectric materials can enable easier manipulation of this intertwined electronic state [6]. Therefore, ferromagnetic and ferroelectric materials have been actively searched for. However, the coexistence of ferromagnetism and ferroelectricity has been rarely observed in bulk forms. This is generally because the unpaired electrons of transition metal ions necessary for magnetism disfavor the off-center ionic displacement required for ferroelectricity [7].

The ferromagnetic moments in magnetoelectric compounds have thus been scrutinized in heterostructures such as thin films [8] and composite magnetoelectric materials [9] by combining several phases with desired properties. Nevertheless, numerous factors such as complex growth processes and effects of interfaces and substrates make experiments and their analyses more challenging and less straightforward. On the other hand, ferrimagnets, where the ferromagnetic moment is uncompensated owing to dissimilar sizes of opposite magnetic moments, can be suitably alternative systems. They are also promising for spintronics applications since they possess both

*Present address: Forschungszentrum Jülich, Lichtenbergstrasse 1, 85747 Garching, Germany.
†Contact author: sungkyunchoi@ibs.re.kr

ferromagnetic and antiferromagnetic properties [10]. Therefore, identifying and understanding magnetoelectric systems with a ferromagnetic moment in a single phase is of significant importance. It also holds promise for technological applications, such as energy-efficient functional devices [11,12].

A series of honeycomb-based magnetoelectric antiferromagnets, $\mathcal{A}_4\mathcal{B}_2O_9$ ($\mathcal{A}$ = Mn, Fe, and Co, and $\mathcal{B}$ = Nb and Ta) [13], could be potentially relevant in this respect. These materials have attracted considerable attention in recent years owing to their wide range of intriguing magnetoelectric properties. These include magnetodielectric effects in $Mn_4Nb_2O_9$ [14], anisotropic magnetoelectricity in $Mn_4Ta_2O_9$ [15], nonlinear ME effects in $Fe_4Nb_2O_9$ [16], coexistence of type-II multiferroicity and linear magnetoelectricity in $Fe_4Ta_2O_9$ [17], manipulation of electric polarization with a rotating magnetic field within the honeycomb plane in $Co_4Nb_2O_9$ [18], and nonlinear and anisotropic ME effects in $Co_4Ta_2O_9$ [19].

In contrast to their diverse magnetoelectric properties, the compound family is all antiferromagnetically ordered at temperatures below about 20−108 K [15–26]. However, the magnetic properties at lower temperatures within the antiferromagnetic order are different. Remarkably, $Co_4Ta_2O_9$ [19,23] and $Mn_4Ta_2O_9$ [15] single crystals exhibit sudden upward turns in magnetic susceptibility at approximately 6 K [23] and 48 K [15], respectively. A peak in magnetic susceptibility in polycrystalline $Mn_4Nb_2O_9$ powder was also observed at approximately 45 K [25]. The upturn in magnetic susceptibility is reminiscent of the onset of the ferromagnetic moment [27]. However, it is unclear whether this characteristic is genuine, and what causes it.

Herein, we tackle this problem by examining high-quality $Co_4Ta_2O_9$ single crystals. We report an intrinsic ferromagnetic moment at low temperatures via dc and ac magnetic susceptibility, magnetization, and neutron diffraction measurements on identical single crystals. The low-temperature magnetic anomaly showed a periodic magnetic anisotropy within the trigonal plane and was frequency independent. The signal was observed in a monostructural domain crystal, but it was nearly absent in a multistructural domain crystal. These observations are consistent with the presence of an intrinsic ferromagnetic moment, which can be used as a control knob to manipulate the magnetoelectric state. The ferromagnetic moment was close to isotropic in magnetization measurements. Assisted by the group theory analysis, it means that the magnetic ground state should belong to a $P1$ magnetic space group. This is the first direct demonstration of the magnetic state that has only a translational symmetry. It implies that physical activities are allowed along any crystallographic directions, by thereby explaining an unusual magnetoelectric effect observed in $Co_4Ta_2O_9$, allowing all three ME mechanisms. According to the magnetic point group (MPG), the ground state belongs to an M-type altermagnet, where theory predicts intriguing physical properties for observations, such as various linear ME, electric polarization, optical, and second-harmonic generation effects. Our results underscore the complexity of magnetic properties and emphasize the need for a thorough investigation of $\mathcal{A}_4\mathcal{B}_2O_9$ ($\mathcal{A}$ = Mn, Fe, and Co, and $\mathcal{B}$ = Nb and Ta) to determine the magnetic ground state and understand their unconventional magnetoelectric properties, by providing related materials to search for the ferromagnetic moment in magnetoelectric systems or $P1$ magnetic space group.

The rest of this paper is organized as follows: Section II provides a detailed description of the dc and ac magnetic susceptibility and neutron diffraction measurement. Section III explains the crystal structure. Section IV presents the magnetic susceptibility results for the dc mode (Secs. IV A and IV B), ac mode (Sec. IV C), and magnetization (Sec. V). The neutron diffraction results are presented in Sec. VI. We discuss the implications of our observations in Sec. VII and summarize our conclusions in Sec. VIII. The Appendices include additional analysis and information.

II. EXPERIMENTAL DETAILS

$Co_4Ta_2O_9$ single crystals were synthesized using a flux method [19]. We chose seven single crystals by screening several crystals from various batches for systematic and comparative susceptibility measurements. They were labeled as crystals 1–7 (approximately 10–60 mg). The orientation of the crystals was confirmed using Laue x-ray diffraction. The crystallographic c axis is normal to the flat surface, a naturally grown facet. The dc magnetic susceptibility measurements of all seven crystals were performed with a magnetic property measurement system (MPMS)-XL magnetometer using a reciprocating sample option for better sensitivity to the induced magnetic moment. The dc susceptibility measurements were first performed from approximately 2 to 293 K at 0.1 T, and then performed from 2 to 30 K for all crystals. The ac measurements were performed on the three selected single crystals using an MPMS3 with a vibrating sample magnetometer. An oscillating magnetic field (8 Oe) was applied within the ab plane in the frequency range of 50–1000 Hz with a 0.05 T magnetic field.

Neutron diffraction experiments were performed on single crystal diffractometer [28] at ISIS, where the time-of-flight Laue technique was used to access large three-dimensional volumes of reciprocal space in a single measurement. Three crystals (crystals 1, 4, and 7) characterized by their dc and ac magnetic susceptibilities were used for neutron diffraction measurements. Their masses are about 30.4, 22, 24.5 mg, respectively. These were labeled in the order of the strength of the low-temperature magnetic anomaly [see the microscopic images in Figs. 3(a)–3(c) for their shapes and dimensions]. Neutron diffraction measurements were performed in the paramagnetic phase at 25 K. The neutron data on crystals 1 and 7 were collected at two azimuthal rotation angles (3.5 mA with a typical current rate of 170 μA/h), whereas the data for crystal 4 were collected at three azimuthal rotation angles (2.7 mA).

Structural refinements were performed using a JANA2006 software [29]. Extinction corrections were made using the isotropic Becker and Coppens model (a mixed Lorentzian model) implemented in the software [29,30]. Absorption correction was performed analytically using a multifaceted crystal model [31]. The observed peaks with intensities $I > 3.0 \times \sigma(I)$ were utilized in the refinements, where I and $\sigma(I)$ were the intensity and standard deviation, respectively. Crystal 4 has been examined using neutrons in a previous study [23]. For a more accurate analysis, we used three integration

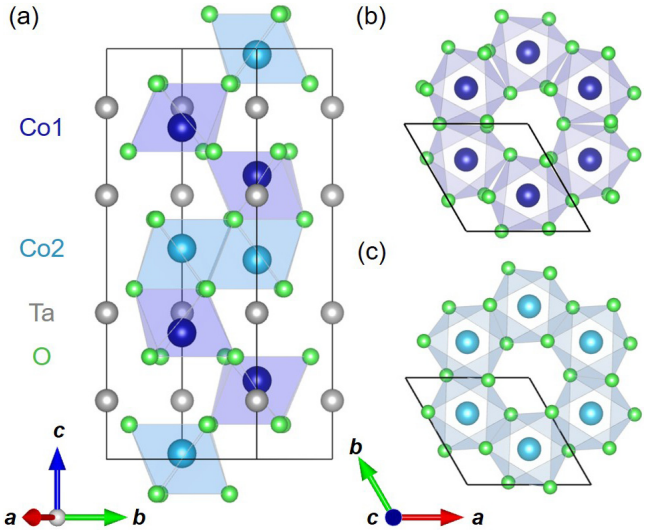

FIG. 1. Crystal structure of $Co_4Ta_2O_9$ determined by neutron diffraction at 25 K [crystal 1, Fig. 7(a)]. (a) Crystallographically distinct Co1 and Co2 sites in a unit cell. (b), (c) The buckled ($0.15 \leqslant z \leqslant 0.35$) and flat ($-0.1 \leqslant z \leqslant 0.1$) honeycomb layer, respectively.

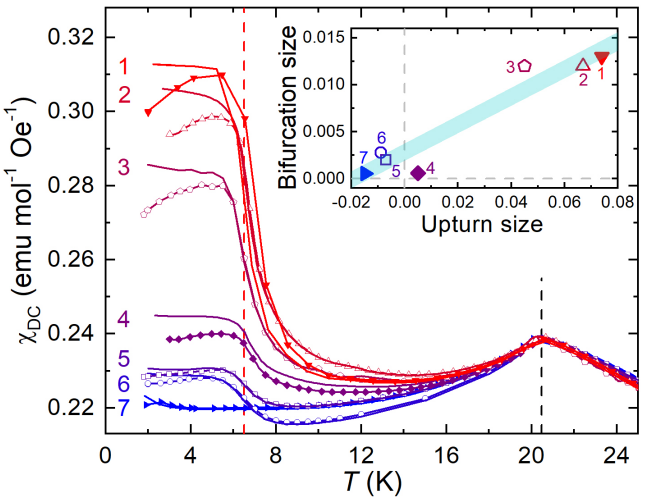

FIG. 2. The dc magnetic susceptibility of seven single crystals. Inset shows the extracted size of the bifurcation as a function of the size of the upturn in susceptibility at the base temperature; filled symbols depict the crystal 1, 4, and 7, chosen for detailed studies in this paper. Line + symbol (pure line) data are represented as ZFC (FC).

methods implemented in an SXD2001 software [32]. Line, box, and volume integration methods, corresponding to one-, two-, and three-dimensional integration, respectively, were tested using 25 K data. Two-dimensional integration data were then chosen because they gave rise to the lowest reliability R(obs) value. The group theory and magnetoelectric tensor analysis were performed using the Bilbao crystallographic server [33].

III. CRYSTAL STRUCTURE

$Co_4Ta_2O_9$ crystallizes in a honeycomb-based structure that belongs to $\mathcal{A}_4\mathcal{B}_2O_9$ ($\mathcal{A}$ = Mn, Fe, and Co, and $\mathcal{B}$ = Nb and Ta) [13]. It deviates from the well-known corundum crystal structure, such as Cr_2O_3 [34], where Cr ions are replaced by four Co and two Ta ions.

Figure 1 shows the refined crystal structure obtained at 25 K using neutron diffraction data. $Co_4Ta_2O_9$ possesses two crystallographically distinct sites, Co1 and Co2 [Fig. 1(a)], where Co1 ions form a buckled honeycomb lattice [Fig. 1(b)], and Co2 ions make a layered honeycomb lattice [Fig. 1(c)]. A face-sharing octahedra is formed in three dimensions [Fig. 1(a)]. The refined crystal structure is consistent with a structure previously determined at room temperature via x-ray diffraction [19].

IV. MAGNETIC SUSCEPTIBILITY

We performed systematic susceptibility measurements to understand the characteristics of the low-temperature anomalies observed in the flux-grown single crystals [19,23]. Extensive zero-field-cooled (ZFC) and field-cooled (FC) magnetic susceptibilities were measured in dc and ac modes.

A. The dc data

Figure 2 presents the dc magnetic susceptibility (χ) for both ZFC and FC. A dramatic drop in the magnetic susceptibility is commonly observed below the Néel temperature ($T_N \sim 20.3-20.7$ K). In addition, an anomaly is revealed at a lower temperature ($T^* \sim 6.1-6.65$ K). These two characteristic temperatures are denoted by black and red dashed lines, respectively, in Fig. 2; they are consistently denoted in all other figures in this paper. Interestingly, the data at lower temperatures varied with the size of the bifurcation between the ZFC and FC data. Susceptibility at the base temperature showed either a positive or negative value, compared to susceptibility at T_N. Thus, the low-temperature susceptibility anomaly depends on the crystal. From these data, we extracted the size of the ZFC/FC bifurcation and the upturn feature in the susceptibility, as shown in the inset of Fig. 2. The inset clearly shows the linear relationship between these two parameters, which are proportional to each other [see a shaded line in the inset]. Therefore, the larger the bifurcation size, the higher the upturn magnitude of the susceptibility below T_N. Crystals 1, 4, and 7 (marked with solid symbols in an inset of Fig. 2) were selected based on this observation to perform the detailed ac and dc susceptibility measurement with the rotating magnetic field within the *ab* plane to learn about the magnetic anisotropy.

B. Direction-dependent dc data

We collected x-ray Laue and neutron diffraction data from three representative samples, crystals 1, 4, and 7. The Laue data show the same sixfold symmetry within the *ab* plane, as shown in Figs. 3(a)–3(c). After confirming the in-plane orientation, systematic magnetic susceptibility measurements were performed.

Figures 3(d)–3(f) present dc magnetic susceptibility data along with all high-symmetric directions in the *ab* plane for both ZFC and FC modes. A common drop in susceptibility is observed at T_N, followed by a characteristic upturn near

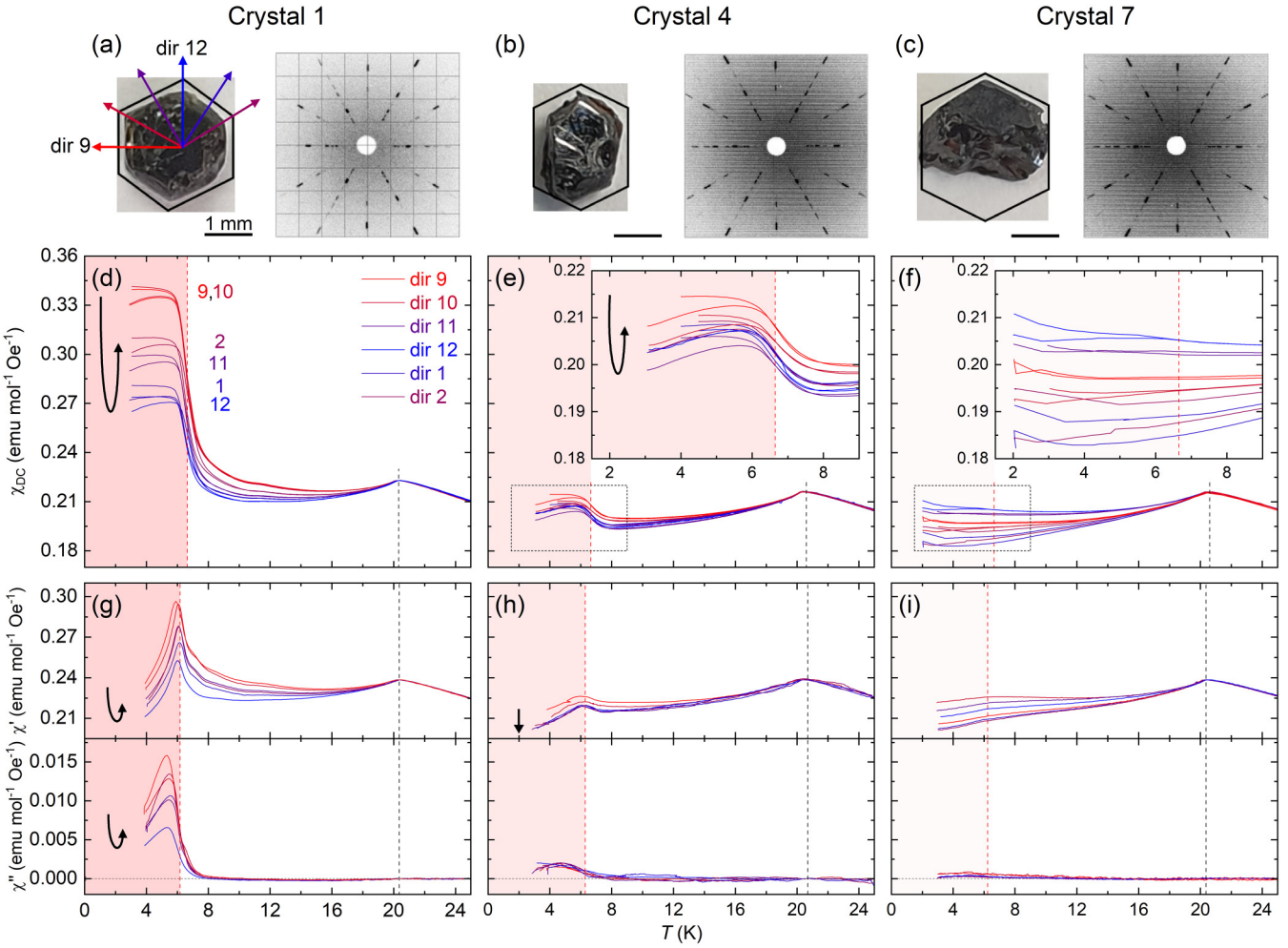

FIG. 3. (a)–(c) Photos and Laue data of crystals 1, 4, and 7, respectively. The two high-symmetric in-plane directions, the directions 9 and 12, are marked in panel (a). (d)–(f) Direction-dependent dc magnetic susceptibility in the *ab* plane. Insets in panels (e) and (f) depict expanded views at the low-temperature region. (g)–(i) Direction-dependent ac magnetic susceptibilities in the *ab* plane at 250 Hz and 8 Oe. The black and red vertical dashed lines in panels (d)–(i) denote the two characteristic temperatures T_N and T^*, respectively. A different transparency of the rectangle below T^* in panels (d)–(i) corresponds to the magnitude of the upturn of the magnetic susceptibility.

T^*. The response diminishes from crystal 1 to 4 and to 7, consistent with Fig. 2. In Fig. 3(d), a strong low-temperature upturn is present in all directions. This feature is enhanced in direction 9 (red solid line), and weakens toward direction 12, but recovers toward direction 3. This trend is consistent with our previous observation from neutron diffraction and magnetic susceptibility measurements [23], where the easy and hard axis of the long-range antiferromagnetic order is along [1 1 0] and [1 −1 0], corresponding to the direction 12 and 9 of crystal 1, respectively. The relative magnitude of the magnetic susceptibility signal below T_N is maintained down to a base temperature measured, regardless of the magnetic field direction [see Fig. 3(d)]. This result indicates that the anisotropy of the noncollinear magnetic order determined at 15 K (below T_N) [23] is likely intact through the low-temperature anomaly. The black arrows in Figs. 3(d) and 3(e) denote the magnetic susceptibility change at the base temperature from directions 9 to 12 and then to 2. Unlike crystals 4 and 7, this tendency was consistent for both dc and ac data for crystal 1, possibly because of the dominant population of a monoclinic magnetic domain [23].

A similar analysis becomes challenging for the other two crystals, crystals 4 [Fig. 3(e)] and 7 [Fig. 3(f)], as the direction-dependent data are less distinguishable. A small increase in magnetic susceptibility is clearly seen in crystal 4 as well [the data below T^* in Fig. 3(e)]. On the other hand, this feature was effectively suppressed in crystal 7, as shown in Fig. 3(f). Thus, the determination of the magnetic anisotropy of crystals 4 and 7 was less reliable.

C. Direction-dependent ac data

To characterize the low-temperature anomaly, we performed ac magnetic susceptibility measurements by tracing the real (χ') and imaginary (χ'') parts. Figures 3(g)–3(i) display the ac data of three crystals. In all crystals, a clear drop in χ' is observed below T_N [black dashed lines in Figs. 3(g)–3(i)], whereas χ'' remains close to zero. This is because the antiferromagnetic domain-wall motion is not driven by an oscillating magnetic field [35], as consistently observed in other antiferromagnetic materials [36].

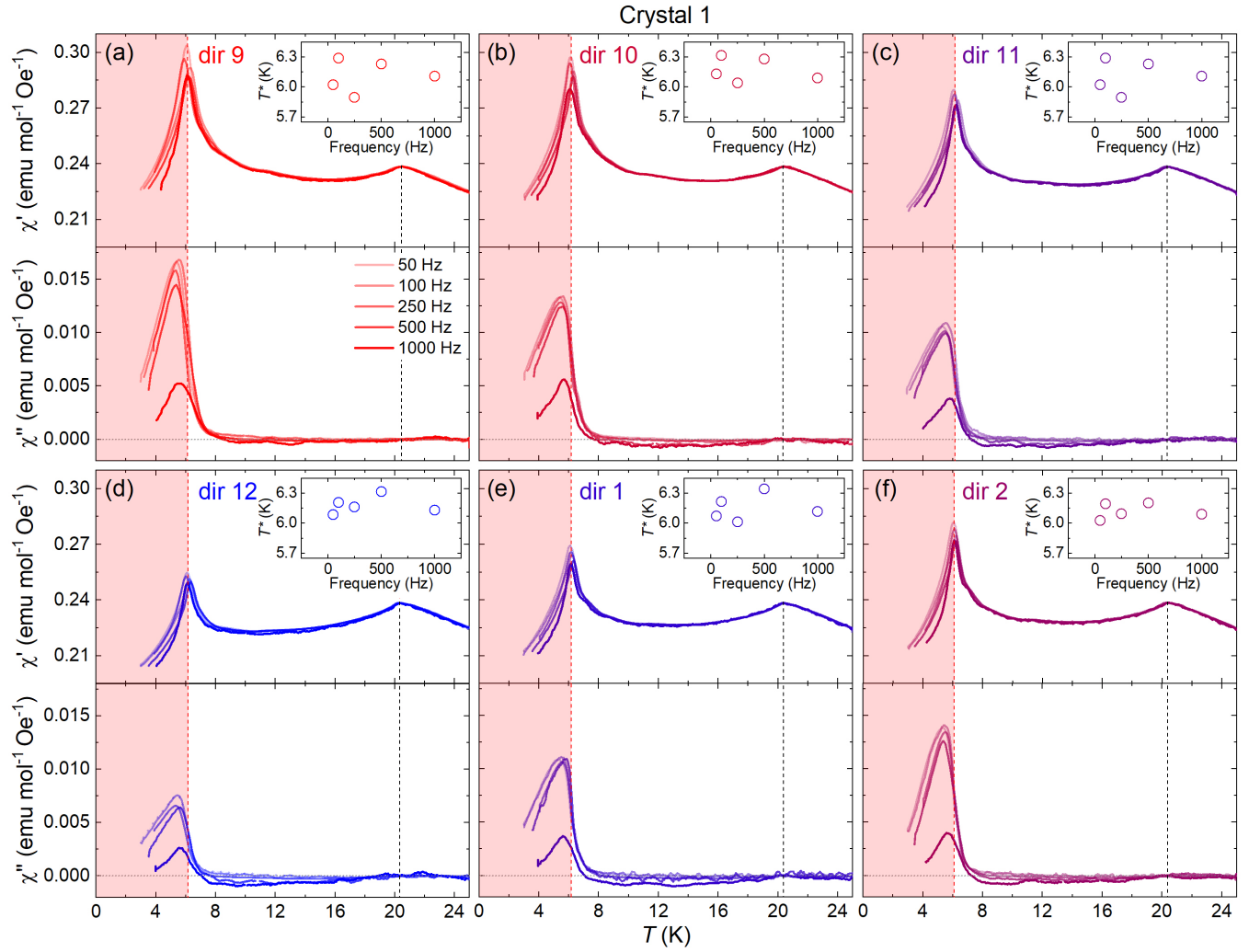

FIG. 4. Direction-dependent ac magnetic susceptibility for crystal 1. In-phase (χ') and out-of-phase (χ'') components are shown in a frequency range from 50 to 1000 Hz along the clockwise direction illustrated in Fig. 3(a). Insets show T^* with frequency.

On the other hand, the ac data reveal an enhanced signal near T^* for both χ' and χ''. As shown in Fig. 3(g) for crystal 1, χ' reveals a sharp peak near T^* (top panel). A broader signal in the χ'' channel (bottom panel) was observed at similar temperatures. This could be consistent with the ferromagnetic moment [37] or a spin glass [35,36] (discussed in Sec. VII).

The low-temperature peak in the ac data for crystal 4 was significantly weaker [Fig. 3(h)], but was still observed. However, this was strongly suppressed in crystal 7 [Fig. 3(i)]. As a result, the low-temperature anomaly in the ac data is consistent with the size of the upturn and bifurcation between ZFC and FC near T^* in the dc data [Figs. 3(d)–3(f)].

To further examine the nature of the low-temperature anomaly found in the magnetic susceptibility, we performed direction-dependent ac measurements on two dissimilar crystals, crystals 1 and 7. The results are summarized in Figs. 4 and 5, respectively.

Figure 4 presents χ' (upper panel) and χ'' (lower panel) with the ac magnetic field applied along the different directions in the *ab* plane at different frequencies from 50 to 1000 Hz. It shows the strongest signal near T^* for both the real and imaginary parts along direction 9 (a hard-axis direction) [Fig. 4(a)], whereas the weakest signal is observed for direction 12 (an easy-axis direction) [Fig. 4(d)]. Thus, χ' decreases from directions 9 to 12 and increases again toward direction 3. This behavior is consistently observed in χ''. This is also consistent with the dc data, as shown in Fig. 3(d). In Fig. 4, χ' is similar regardless of the frequency; a weak trend for the suppression is only observed with increasing frequency. This is similarly observed in χ'' up to 500 Hz, but it decreases at 1000 Hz for all directions. This significant decrease in magnetic loss [37] occurs because a rapidly oscillating magnetic field has lesser effect on the magnetic domain [35]. Insets of Fig. 4 show a rather random distribution of T^* with frequency, disfavoring the spin-glass transition (see Appendix B for the details).

On the other hand, the direction-dependent ac data were distinct for crystal 7, as shown in Fig. 5. The signature of the antiferromagnetic transition at T_N was consistently observed. However, the low-temperature anomaly at around T^* was significantly suppressed. Unlike the crystal 1 data (Fig. 4), χ' along the direction 9 was weak, and did not show a clear sinusoidal trend in the clockwise direction. For direction 9, χ'' shows a continuous decrease with an increasing frequency.

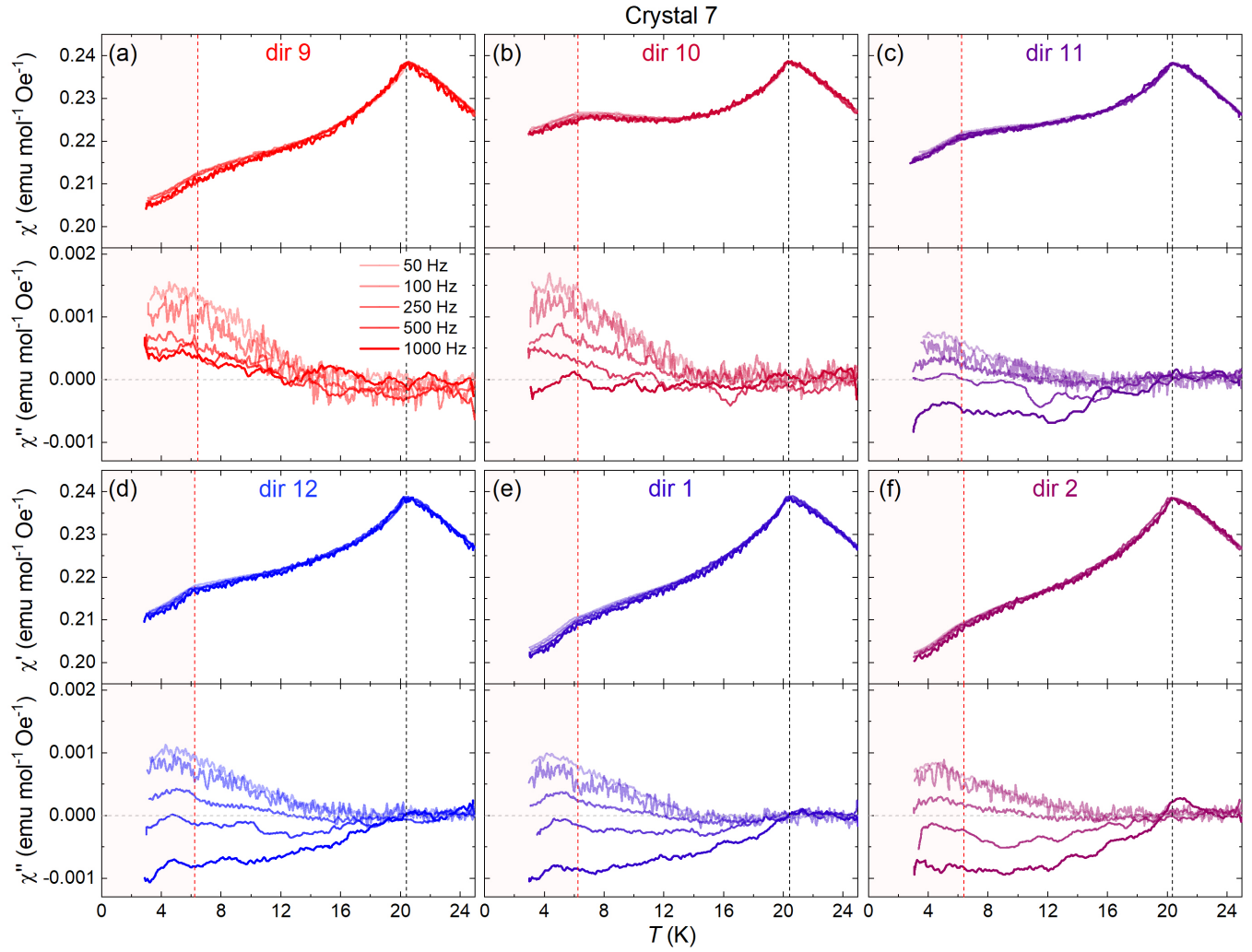

FIG. 5. Direction-dependent ac magnetic susceptibility for crystal 7. In-phase (χ') and out-of-phase (χ'') components are shown in a frequency range from 50 to 1000 Hz along the clockwise direction illustrated in Fig. 3(a).

Notably, χ'' near T^* revealed a strong frequency dependence with the rotating magnetic field within the *ab* plane. It even showed negative signals in directions 11, 12, 1, and 2, at frequencies higher than 250 Hz. The negative χ'' clearly developed below the T_N. In contrast, this behavior was not observed in the other two crystals (1 and 4). It might be attributed to the multistructural domain (to be discussed).

V. MAGNETIZATION

Figure 6 presents the magnetization (M) of crystal 1 as a function of the applied magnetic field (H) at around 2 K (well below T^*) along all high-symmetric directions, same as those in the susceptibility measurements [left panel of Fig. 3(a)]. Figure 6(a) shows a linear magnetization trend in all directions, indicating the dominant antiferromagnetic exchanges. However, a magnetic hysteresis is revealed in the magnified view in Fig. 6(b) for all directions, which is consistent with the ferromagnetic moment observed in the susceptibility measurements [Figs. 3(d), 3(g), and 4]. A magnificated view in Fig. 6(c) shows the feature of a nearly isotropic ferromagnetic moment regardless of the direction of the magnetic field. A similar magnetic hysteresis is observed in the magnetization along the $H \parallel c$ axis at 2 K, with an out-of-plane ferromagnetic moment component, indicating nearly isotropic ferromagnetism below T^* (also see Appendix A and Fig. 9 for the details).

VI. NEUTRON DIFFRACTION

Neutron diffraction measurements were performed to understand the nature of the distinct magnetic susceptibilities of the three crystals. Figure 7 shows the structural refinement results. The nuclear structures of all three crystals were refined at a paramagnetic temperature of 25 K. The refined crystal structure was nearly the same as that obtained in previous studies using neutrons at 25 K [23] and x-rays at room temperature [19]. With the given reflection list, we chose the best isotropic extinction model while fitting the scale factor, followed by refinement of isotropic thermal parameters and atomic positions.

Importantly, refinements with a single structural domain worked well for crystals 1 and 4, as shown in Figs. 7(a) and 7(b). The calculated structure factor (F_{calc}) was very close to

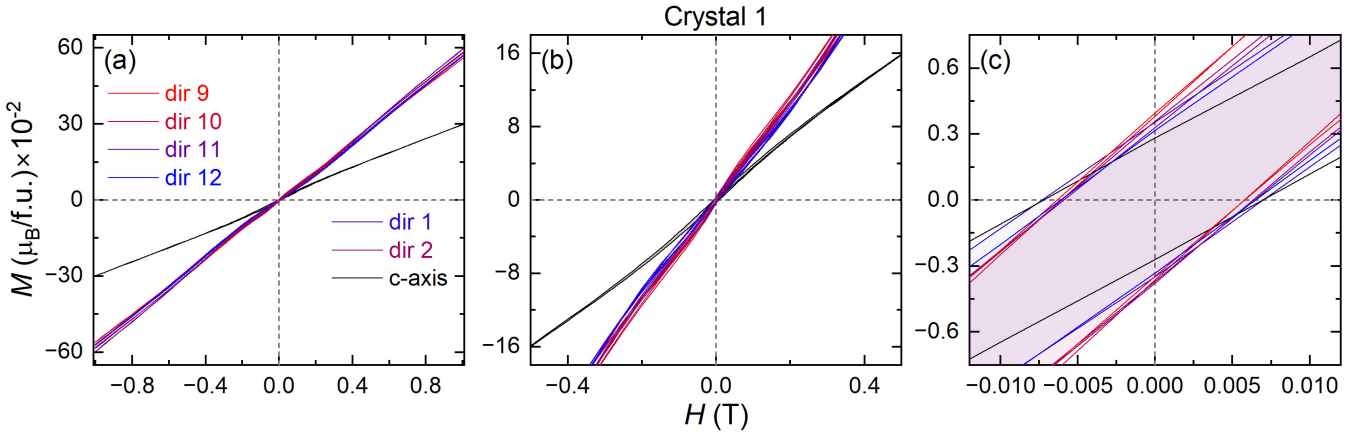

FIG. 6. Magnetization of crystal 1. (a) Comparison of magnetization data. External magnetic fields are applied along both in-plane and out-of-plane directions illustrated in Fig. 3(a). (b) Magnetic hysteresis revealed in an expanded view of panel (a). (c) Nearly isotropic magnetic hysteresis in an further expanded view of panel (b). Hysteresis is denoted through shading for all directions measured.

the observed structure factor (F_{obs}); i.e., the reflection symbols were located very close to the linear line. However, the structural refinement of crystal 7 with a single structural domain was significantly worse, as shown in Fig. 7(c). There is a large number of Bragg reflections whose observed structure factors are stronger than those of the calculated structure factors. This means the remaining of the signal that is not accounted for. However, including the second structural domain significantly improves the fit, as shown in Fig. 7(d).

The two structural domains found in crystal 7 are the same by a vertical mirror symmetry along the a axis in Fig. 7(e), as follows: Domain 1 in Fig. 7(e) is the same as that after a clockwise rotation by 120° with the right-hand rule, as shown in Fig. 7(f). This is because [1 0 0], [0 1 0], and [−1 −1 0] are chemically equivalent by a threefold rotation symmetry along the characteristic $\boldsymbol{c}$ axis of a trigonal unit cell. Domain 1 in Fig. 7(f) is then equivalent to the domain in Fig. 7(g) in terms of a vertical mirror plane along the horizontal direction. This is domain 2, which was revealed by Rietveld refinements in the neutron diffraction analysis [Fig. 7(d)]. That is, the two structural domains are the same by the mirror symmetry. The relationship between two structural domains is given by $\boldsymbol{a}' = \boldsymbol{b}$, $\boldsymbol{b}' = \boldsymbol{a}$, and $\boldsymbol{c}' = \boldsymbol{c}$, and in terms of the reciprocal lattice components $h' = k$, $k' = h$, and $l' = l$, where the prime notation denotes the second structural domain. Note that the definition for the reliability parameter such as R(obs) can be found in the literature [38]. The fitted lattice parameters of crystals 1, 4, and 7 are a = 5.1594(24), c = 14.1225(66) Å, a = 5.1627(22), c = 14.1188(64) Å, and a = 5.1601(21), c = 14.1188(62) Å, respectively, confirming the consistency across samples. The refined nuclear space group $P\bar{3}c1$ is the same for all.

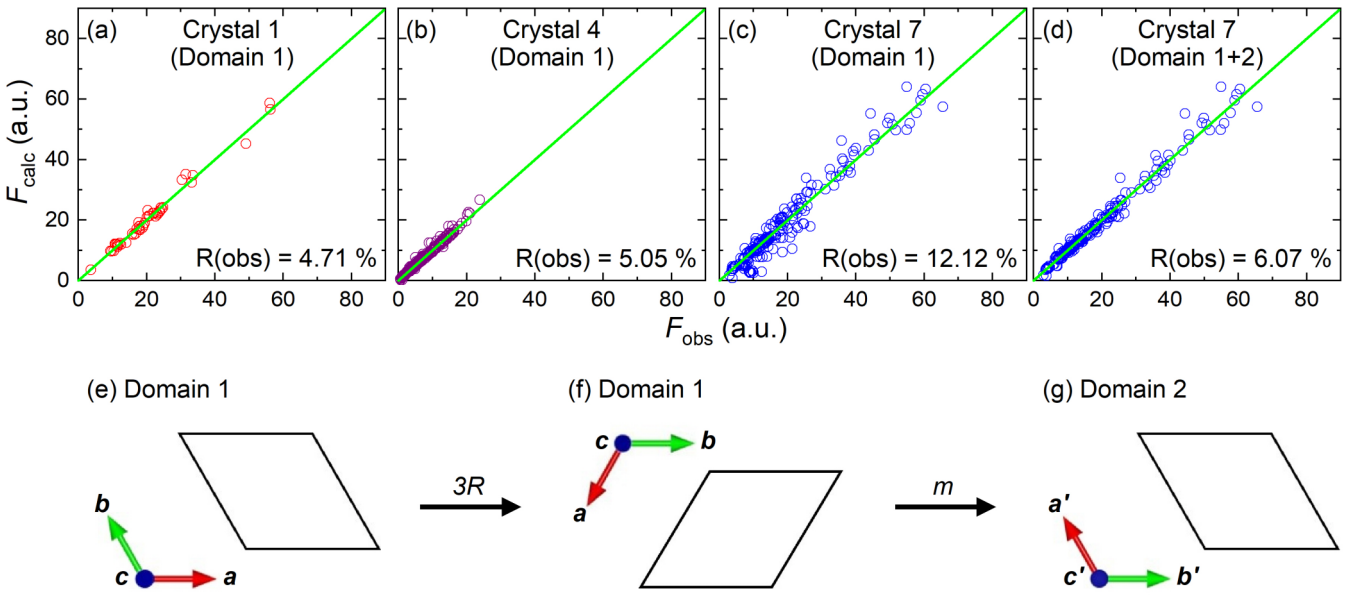

FIG. 7. Structural refinements using neutron diffraction at 25 K for (a) crystal 1, (b) crystal 4, and (c), (d) crystal 7. A monostructural domain was used in panels (a)–(c), whereas two domains were used in panel (d). The crystal 4 data were replotted based on a previous study [23]. (e)–(g) The unit cell transformation from domain 1 to 2.

VII. DISCUSSION

In this study, we performed in-depth magnetic susceptibility and neutron diffraction measurements on identical $Co_4Ta_2O_9$ crystals to understand low-temperature anomalies found in magnetic susceptibility. The increase and ZFC/FC bifurcation in the magnetic susceptibility below T^* could be due to a weak ferromagnetic moment or spin glass. Crystals 1 and 4 had monostructural domains, as determined by neutron diffraction. For those crystals, an upturn in the magnetic susceptibility below T^* was detected up to 1000 Hz [see Figs. 3(d), 3(e), 3(g), 3(h), and 4]. T^* did not show any meaningful change with frequency for all directions in the *ab* plane for crystal 1 (see insets of Fig. 4). This is less compatible with a spin-glass phase [36,39]. A short-range order with spin clusters would be present in the spin-glass state with its relaxation time [39]. This can be deduced from the Argand plot and nonlinear susceptibilities [36,40], but our data did not observe such characteristics (see Appendix B and Fig. 10 for the details). Crystal 7 has two structural domains, with the second domain comprising approximately 20% and exhibiting significantly suppressed magnetic susceptibility [Figs. 3(f), 3(i), and 5]. In addition, if the T^* anomaly were due to a spin glass with random spins, the multistructural domains would not necessarily affect the low-temperature feature in magnetic susceptibility. Thus, our results indicate that the contribution from a spin-glass phase below T^* would be minor even if present.

Instead, our data are more consistent with ferromagnetic moments [36]. The low-temperature magnetic anomaly followed an intrinsic magnetic anisotropy of the antiferromagnetic state below T_N in both dc and ac data [Figs. 3(d), 3(g), and 4]. χ'' in the ac magnetic susceptibility showed a peak at around T^* [Figs. 3(g) and 4]. This observation can be understood through domain walls in ferromagnets affected by an oscillating magnetic field, which have some characteristic timescale yielding the χ'' in the ac measurement [35]. In contrast, the low-temperature anomaly was nearly absent in crystal 7, which contains two structural domains. Interestingly, χ'' reveals a sign change from a positive to negative signal with frequency, which was not observed in the other two crystals. This might be explained by the more complex magnetic domain-wall structures originating from multistructural domains; in principle, six magnetic domains can be realized from two structural domains for crystal 7. Magnetic domain-wall motion [36] may be associated with this phenomenon. Our results suggest that the absence of the low-temperature magnetic anomaly in crystal 7 is likely due to a multidomain effect, smearing the intrinsic magnetic properties shown in crystals 1 and 4. The role of multistructural domains in magnetic properties can be elucidated using our findings. When two structural domains are equally populated (50% each), the out-of-plane ferromagnetic moment cancels due to the reversed *c* axis. Similarly, the in-plane ferromagnetic moment also cancels. However, the in-plane ferromagnetic moment can experience partial cancellation, as it does not undergo the same inverse transformation as the out-of-plane ferromagnetic component. This explanation assumes a single antiferromagnetic domain formed from a single structural trigonal domain. In reality, three antiferromagnetic domains can arise from the single structural trigonal domain, further diminishing the in-plane ferromagnetic moment. This can account for the nearly absent T^* anomaly in crystal 7, compared to crystal 1. In this mechanism, multistructural domains significantly influence the intrinsic low-temperature magnetic properties by destabilizing the ferromagnetic moment below T^*. Consequently, the ferromagnetic moment can exist in high-quality $Co_4Ta_2O_9$ single crystals. Further investigation of the ferromagnetic moment and its characteristics in high-quality $Co_4Ta_2O_9$ single crystals, particularly regarding multistructural domains, will be insightful using complementary experimental techniques such as coherent x-ray scattering, transmission electron microscopy, magnetic force microscopy, or the magneto-optical Kerr effect in future studies.

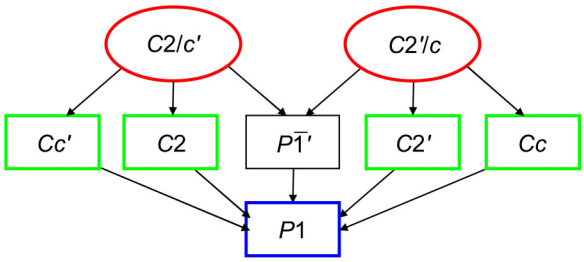

FIG. 8. Group-subgroup diagram. A hierarchy of magnetic space groups is displayed from $C2/c'$ and $C2'/c$ to the lowest possible group $P1$. Five magnetic space groups, which support a ferromagnetic moment, are depicted with green and blue rectangles.

We further performed the group theory analysis to understand the magnetic ground state. Two primary magnetic space groups, $C2/c'$ (No. 15.88) and $C2'/c$ (No. 15.87) (two red ellipsoids in Fig. 8), were previously considered at 15 K in $Co_4Ta_2O_9$ [23]. However, both do not support a ferromagnetic moment and thus cannot be the magnetic space group below T^*. To find the magnetic ground state below T^*, a subgroup analysis was performed by lowering the symmetry from two magnetic space groups, as illustrated in Fig. 8. Accordingly, six magnetic space groups with lower symmetries were obtained. Among them, five candidates, Cc' (No. 9.39), $C2$ (No. 5.13), $C2'$ (No. 5.15), Cc (No. 9.37) (green rectangles in Fig. 8), and $P1$ (No. 1.1) (a blue rectangle in Fig. 8), can support the ferromagnetic moment. None of them have an inversion symmetry, which allows the finite electric polarization at zero magnetic fields. This sharply contrasts the current consensus on the linear magnetoelectricity in $Co_4Ta_2O_9$ below T_N. The symmetrically allowed components of the ME tensor for all five magnetic space groups were obtained via group theory analysis, as listed in Table I.

A nearly isotropic ferromagnetic moment was observed in magnetization measurements [see Fig. 6(c)]. The magnetic point groups of the five magnetic space groups found in this study are m', $2'$, m, 2, and 1. The very first (the next) two cannot have a ferromagnetic moment along (perpendicular to) the y axis as it is canceled by the given symmetry. As a result, a ferromagnetic moment having all three components is only compatible with $P1$, the lowest possible magnetic space group. Moreover, $P1$ is consistent with the reported polarization in $Co_4Ta_2O_9$ [19]. The electric polarization in $Co_4Ta_2O_9$

TABLE I. The ME tensors of five candidate groups at a zero magnetic field. The tensor is defined as $P_i = \alpha_{ij} H_j$, where P_i (H_j) is the electric polarization (magnetic field) along the principal direction i (j). The principal axes are [1 1 0], [1 −1 0], and [0 0 1] in the trigonal lattice.

Cc' (No. 9.39) MPG: m'	Cc (No. 9.37) MPG: m	$C2'$ (No. 5.15) MPG: $2'$	$C2$ (No. 5.13) MPG: 2	$P1$ (No. 1.1) MPG: 1
$\begin{bmatrix} \alpha_{11} & 0 & \alpha_{13} \\ 0 & \alpha_{22} & 0 \\ \alpha_{31} & 0 & \alpha_{33} \end{bmatrix}$	$\begin{bmatrix} 0 & \alpha_{12} & 0 \\ \alpha_{21} & 0 & \alpha_{23} \\ 0 & \alpha_{32} & 0 \end{bmatrix}$	$\begin{bmatrix} 0 & \alpha_{12} & 0 \\ \alpha_{21} & 0 & \alpha_{23} \\ 0 & \alpha_{32} & 0 \end{bmatrix}$	$\begin{bmatrix} \alpha_{11} & 0 & \alpha_{13} \\ 0 & \alpha_{22} & 0 \\ \alpha_{31} & 0 & \alpha_{33} \end{bmatrix}$	$\begin{bmatrix} \alpha_{11} & \alpha_{12} & \alpha_{13} \\ \alpha_{21} & \alpha_{22} & \alpha_{23} \\ \alpha_{31} & \alpha_{32} & \alpha_{33} \end{bmatrix}$

[19] showed a dominant signal along the a axis (equally [1 1 0] in the trigonal lattice notation) under an applied magnetic field along all three principal axes. In contrast, all the remaining components of the ME tensor revealed weak but finite values; all the nine components were experimentally observed. Thus, only $P1$ can be compatible with it (see Table I).

The characteristics of the ferromagnetic moment deviating from the noncollinear antiferromagnetic order of $Co_4Ta_2O_9$ below T^* require careful analysis. In a simple ferromagnetic material, all magnetic moments within the unit cell align parallel, creating rotational symmetry in the magnetic unit cell. However, $Co_4Ta_2O_9$ first forms a noncollinear antiferromagnetic order below T_N (see Fig. 6 of Ref. [23]). In this phase, the moments cancel within the magnetic unit cell, resulting in no net ferromagnetic moment. A ferromagnetic moment appearing below T^* is likely that the moments are slightly tilted from the antiferromagnetic arrangement. The magnetic space group changes from $C2'/c$ to $P1$ to account for the intrinsic nearly isotropic ferromagnetic moment. In the $P1$ space group, only translation symmetry remains, allowing the net ferromagnetic moment to point along any direction in three-dimensional space. Consequently, this configuration differs from that of a simple ferromagnetic system.

The $P1$ magnetic space group can be compatible with all three types of magnetic-order-induced ME mechanisms, such as Dzyaloshinskii-Moriya interaction [41], exchange striction [42], and p-d hybridization between magnetic and ligand ions [43]. The magnetic ground state in the $P1$ magnetic space group means that there is only a translational symmetry. This means that various physical properties, such as longitudinal/transverse linear ME, electric polarization, optical, and second-harmonic generation activities [44], are allowed along any direction in principle in this material. Such studies are expected to help understand the nature of the magnetic ground state and the main magnetoelectric mechanism.

Examining the relationship between the ferromagnetic moment and the magnetoelectric properties of $Co_4Ta_2O_9$ will be helpful for guiding future studies. A prior investigation identified unusual ME properties mostly within the ab plane [19]. This observation was explained through a spin-flop scheme and symmetry analysis for a noncollinear magnetic order below T_N [23]. The present study explores a low-temperature magnetic anomaly previously overlooked in the literature, suggesting a net ferromagnetic moment below T^* for the high-quality $Co_4Ta_2O_9$ single crystal. Since the measured polarization occurred at high magnetic fields in the spin-flop state [19], the ferromagnetic moment under ambient conditions may not relate to the observed magnetoelectric effect. However, the ME properties below the critical magnetic field for the spin-flop transition may need to be reexamined, although detecting a meaningful signal would be technically challenging. Based on our group theory analysis using the ferromagnetic moment, electric polarization can arise in high-quality $Co_4Ta_2O_9$ single crystals even without the application of a magnetic field. This imply a possible manipulation of the ME properties by applying a weak magnetic field using the ferromagnetic moment. This possibility warrants further investigation in high-quality $Co_4Ta_2O_9$ crystals.

In contrast, $Co_4Nb_2O_9$ does not show this low-temperature anomaly in the form of both polycrystalline powder [45] and single crystals [20]. Based on our results for $Co_4Ta_2O_9$, this might mean that $Co_4Nb_2O_9$ is more likely to have multiple domains. This may also explain different ME properties in $Co_4Ta_2O_9$ [19] and $Co_4Nb_2O_9$ [20], where the possible effect of multiple domains has been suggested for the latter [20]. Thus careful investigation of the polarization in $Co_4Nb_2O_9$ and $Co_4Ta_2O_9$ single crystals with mono- and multistructural domains would be interesting for future studies.

Similar low-temperature anomalies were also observed in the magnetic susceptibility data of Mn-based compounds. $Mn_4Ta_2O_9$ single crystals [15] exhibited a low-temperature ZFC/FC bifurcation, whereas both $Mn_4Nb_2O_9$ polycrystalline powder [14] and single crystals [46] did not. The multidomain mechanism may also play a role in Mn-based systems. This possibility warrants the subsequent examination of Mn-based compounds.

Recently, altermagnetism has been discovered as an unconventional magnetic class [47]. It is defined as a magnetic state in which spins are fully compensated, but the parity times time-reversal symmetry (PT) is broken [47,48]. All five MPGs found in this study belong to M-type [49], where M means the uncompensated magnetization in the ground state. Theories have predicted unique physical properties such as nonreciprocal Faraday optical rotation and the linear anomalous Hall effect [48,49]. Therefore, they can be the subject of future work, and it will be intriguing to investigate these properties in $Co_4Ta_2O_9$.

VIII. CONCLUSIONS

This paper reported and examined the low-temperature magnetic anomaly and the magnetic ground state of the magnetoelectric $Co_4Ta_2O_9$. We performed detailed magnetic susceptibility, magnetization, and neutron diffraction measurements on identical single crystals, complementary by the

group theory analysis. The magnetic susceptibility peak in both dc and ac data showed a sinusoidal magnetic anisotropy within the *ab* plane for the high-quality crystal. Also, the temperature of the ac susceptibility peak did not change by the external frequency. Further, the low-temperature magnetic anomaly was observed in the monostructural domain crystal, which had a high quality, whereas a multidomain crystal suppressed it. Thus, our combined susceptibility and neutron diffraction results support an intrinsic ferromagnetic moment rather than a spin-glass state. The intrinsic ferromagnetic moment can be used to manipulate the magnetoelectric properties of $Co_4Ta_2O_9$ by an external field. Magnetization measurements revealed a nearly isotropic ferromagnetic moment, which is only consistent with the $P1$ magnetic space group. This indicates that physical activities are allowed in any crystallographic direction, explaining the unusual magnetoelectricity in $Co_4Ta_2O_9$. The group theory predicted the M-type altermagnetic properties of $Co_4Ta_2O_9$, which will be worth investigating. Also, related materials were suggested by bringing an opportunity to search for and examine largely unexplored physical properties from the $P1$ magnetic symmetry or ferromagnetic moments in magnetoelectric materials. Our comprehensive findings warrant careful investigations of $\mathcal{A}_4\mathcal{B}_2O_9$ ($\mathcal{A}$ = Mn, Fe, and Co, and $\mathcal{B}$ = Nb and Ta) to resolve a controversy on the magnetic ground state and figure out their unconventional magnetoelectric properties in the future.

ACKNOWLEDGMENTS

We thank Gisela Schütz and Eberhard Goering for supporting the susceptibility measurements using MPMS and Jongho Park for help with LAUE measurements. This work was supported by the Institute for Basic Science (Grants No. IBS-R011-Y3 and No. IBS-R034-Y1) and Advanced Facility Center for Quantum Technology at Sungkyunkwan University. Part of this study has been performed using facilities at IBS Center for Correlated Electron Systems, Seoul National University. The work at Yonsei was supported by the National Research Foundation of Korea (NRF) through Grants No. RS-2021-NR058241 and No. RS-2022-NR069338. The work at Rutgers University was supported by the DOE under Grant No. DE-FG02-07ER46382.

DATA AVAILABILITY

The neutron diffraction (SXD, proposal No. RB2000175 [50]) presented in this work is available in the ISIS database. The data are available from the corresponding author upon reasonable request.

APPENDIX A: DC DATA

This Appendix presents measurements of magnetic susceptibility and magnetization for the three single crystals, with the applied magnetic field oriented along the c axis. The motivation is twofold: First, these measurements can be more accurate than in-plane measurements due to the better alignment; second, the unique out-of-plane direction allows for an unambiguous comparison of magnetic hysteresis across the three crystals by avoiding an uncertainty present in the magnetic anisotropy within the *ab* plane. Consequently, small magnetic hysteresis can be more effectively characterized.

Figure 9 presents results, finding consistent susceptibility and magnetization below T^*. Figures 9(a)–9(c) show that the upturn feature below T^* is most (least) pronounced for crystal 1 (7), while crystal 4 exhibits an intermediate behavior. The trend in out-of-plane magnetic anisotropy aligns with that of in-plane magnetic anisotropy, as illustrated in Fig. 3. The out-of-plane magnetic susceptibility is consistently lower than the in-plane susceptibility in all samples [Figs. 9(a)–9(c)]. This is also compatible with the magnetization of crystal 1, as shown in Figs. 6(a) and 6(b).

Examining the magnetization data reveals magnetic hysteresis. Figures 9(d)–9(f) illustrate the dependence of magnetization on temperature for the three crystals. A clear pattern is found: Magnetization increases as temperature decreases, indicating stronger magnetic hysteresis below T^*. This trend is further clarified in the enlarged views in Figs. 9(g)–9(i). All crystals display significantly greater magnetic hysteresis at 2 K. The hysteresis magnitude decreases from crystals 1 to 4 to 7, corresponding to the upturn feature near T^* in susceptibility, as shown in Figs. 9(a)–9(c). Thus, the small magnetic hysteresis detected only below T^* is indeed magnetic. Note that minimal constant hysteresis was observed at 12, 25, and 100 K across all samples, likely within experimental error [Figs. 9(g)–9(i)]; see the differences in magnetic hysteresis in Figs. 6(c) and 9(g) from the identical crystal 1, where the latter exhibits a reduced loop. This discrepancy suggests that the measurement uncertainty is comparable to the size of the hysteresis observed at temperatures above T^* [Figs. 9(g)–9(i)].

APPENDIX B: AC DATA

This Appendix presents the spin-glass analysis using the ac data collected from crystals 1 and 7, by excluding the possibility of its dominant contribution below T^* in $Co_4Ta_2O_9$.

In spin-glass materials [35,36,51], the magnetic moments become frozen below the freezing temperature (T_f), and peaks appear in the χ' and χ'' data. T_f is the temperature at the peak in χ', which corresponds to an inflection point in χ''. There are two standard methods to analyze the spin glass using ac magnetic susceptibility data in the literature [35,36,51]. First, as the frequency increases, the freezing temperature monotonically rises because the moments freeze at higher temperatures. Second, a semicircle feature is typically observed in the Argand diagram for the spin glass (also known as the Cole-Cole plot), which plots χ' versus χ'' at different frequencies at a certain temperature. The distribution of relaxation times and its properties can be determined by fitting the diagram.

In this study, both methods were used with the collected ac data. The change of T_f with increasing frequency for crystal 1 is shown in insets of Fig. 4. As one can see, they do not show any systematic trend with frequency, but reveal a rather random distribution. This is inconsistent with the spin-glass transition found in the ac data in the literature [35,36,51]. To further explore the possibility of a spin-glass transition below T^* in $Co_4Ta_2O_9$, we also plotted Argand diagrams for all measured directions for crystals 1 and 7

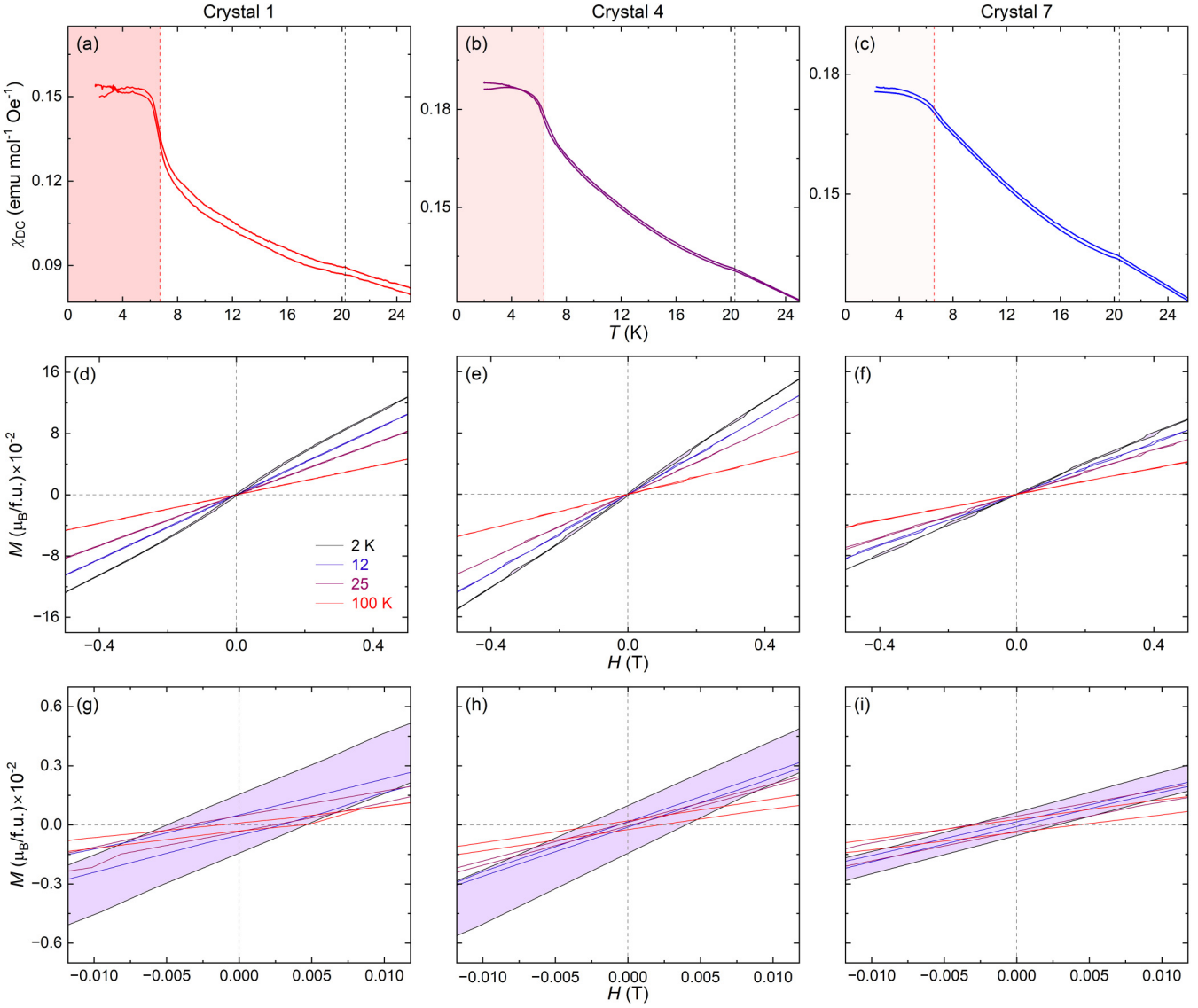

FIG. 9. Magnetic susceptibility and magnetization of three single crystals at $H \parallel c$ axis. (a)–(c) Magnetic susceptibility for both ZFC and FC data. (d)–(f) Magnetization with cooling. (g)–(i) Expanded views of panels (d)–(f). Hysteresis is denoted through shading at 2 K.

using the ac data of Figs. 4 and 5, respectively. Figure 10 presents Argand diagram. As one can see in Fig. 10, no clear trend was observed. Instead of a semicircle, distorted features are found. Therefore, no reliable and systematic observations were found for the spin-glass transition below T^* in $Co_4Ta_2O_9$.

APPENDIX C: INVESTIGATION OF MISALIGNMENTS AND ERROR BARS IN IN-PLANE SUSCEPTIBILITY

For completeness, we provide details for the experimental alignment and error margins related to the out-of-plane tilting of the sample during in-plane magnetometry measurements (Figs. 3–5). The intrinsic cause may stem from slight tilting of the crystal's intrinsic plane. However, this possibility was ruled out, as the natural surface facets of the three single crystals were nearly perfectly aligned with the *ab* plane. This might not be surprising as they were grown by flux growth with natural *ab*-plane facets. Laue measurements in the right panel of Figs. 3(a)–3(c) confirm it.

On the other hand, an extrinsic cause may be a minor tilt when mounting the crystal on the holder with GE varnish. Despite efforts to keep the crystal surface parallel to the holder, some misalignments cannot be entirely excluded. Moreover, another extrinsic effect may arise from slight misalignment of the applied magnetic field to the high-symmetric direction within the *ab* plane of the crystal. To estimate the potential error from these misalignments in in-plane susceptibility measurements, we repeated measurements for crystal 1 three times and averaged the results, as depicted in Fig. 3(d). The standard deviation of the data was only about 2.7%. These measurements confirm the reliable data for crystal 1. Note that measurements for the other two crystals were not repeated due to the minimal differences in data across various directions, complicating the identification of the easy and hard axes of the in-plane magnetic anisotropy.

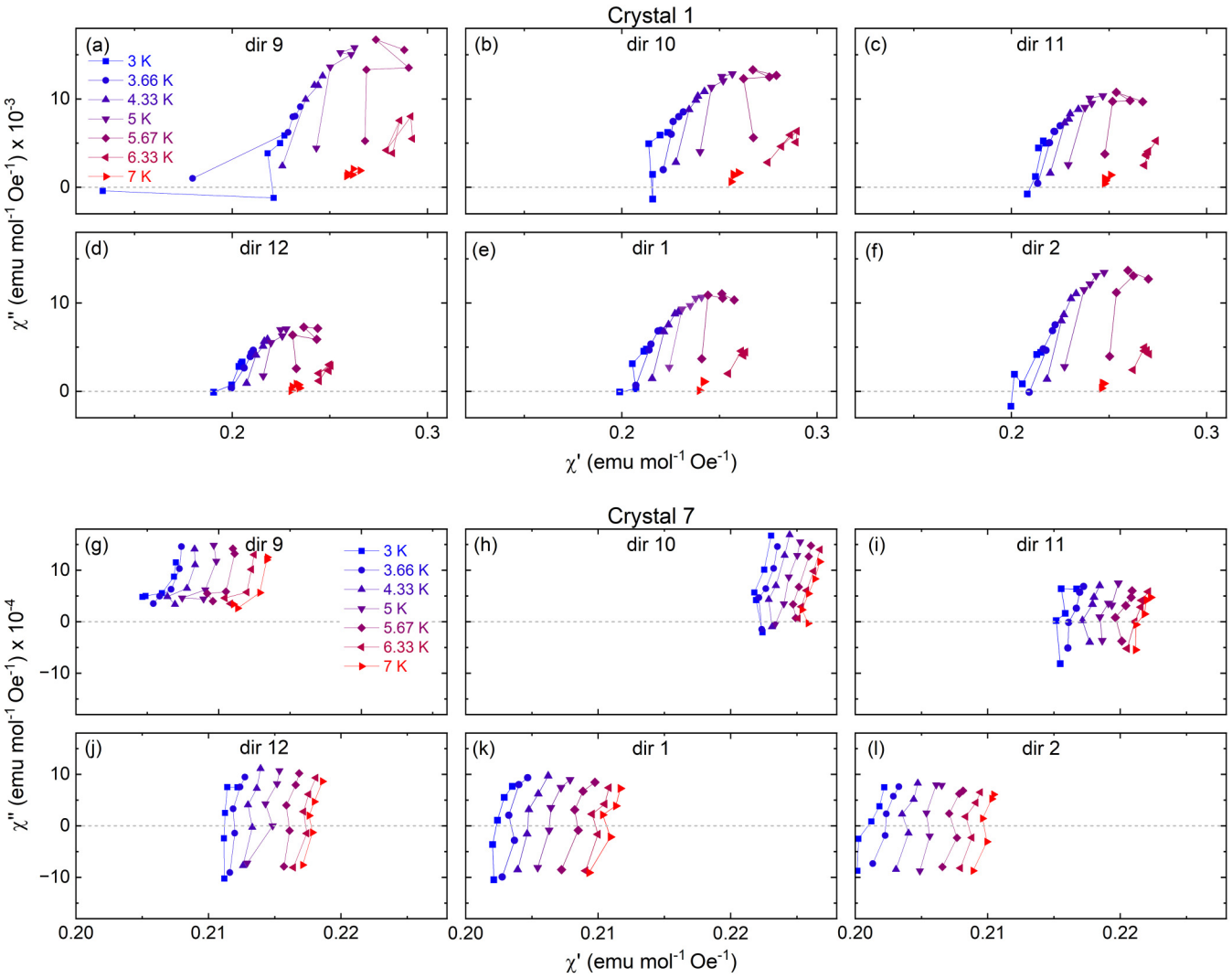

FIG. 10. Argand diagram with varying frequencies at a fixed temperature. (a)–(f) Crystal 1 (Fig. 4). (g)–(l) Crystal 7 (Fig. 5).

APPENDIX D: NEUTRON DIFFRACTION

In this Appendix, we present the results of the structural refinement using the same ten Bragg peaks from crystals 1 and 7 for more direct comparison. Figure 11 displays the comparison of results. Since crystals 1 and 7 were measured simultaneously by neutrons, this comparison is particularly relevant. Utilizing the same Bragg peaks for both crystals enhances clarity in evaluating the impact of the second structural domain on the fit. In Fig. 11(a), R(obs) is 4.11%, lower than

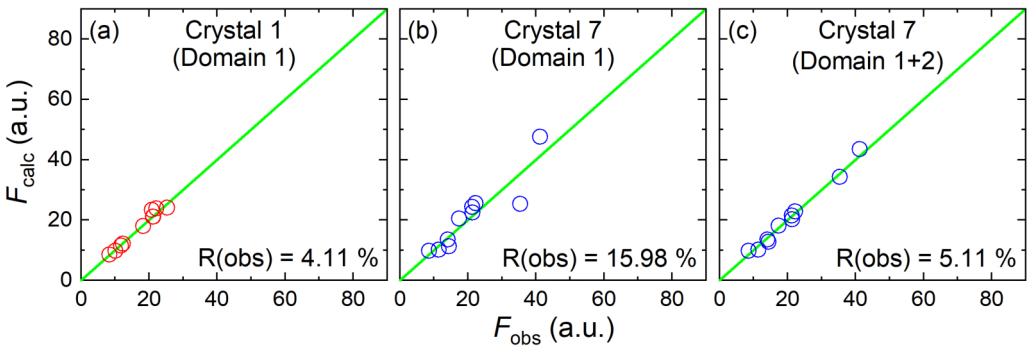

FIG. 11. Structural refinement using the common Bragg peaks. (a) Crystal 1 with mono domain. (b), (c) Crystal 7 with mono and two domains.

the 4.71% in Fig. 7(a). On the other hand, R(obs) for crystal 7 with domain 1 significantly increases from 12.12% in Fig. 7(c) to 15.98% in Fig. 11(b). By including the second structural domain in the fit, R(obs) then decreases largely; specifically, 15.98%−5.11% = 10.87%. The reduction in R factors upon the inclusion of the second domain exceeds that in Figs. 7(c) and 7(d). Thus, our refined analysis with the same peaks demonstrates increased sensitivity to the second structural domain. This finding is consistent with the different observed intensities of the common Bragg peaks (and subsequently their structure factors in refinements) between the mono domain (crystal 1) and two domains (crystal 7). Note that the relative orientations of these two crystals differed, resulting in few common peaks. The ten common peaks identified from crystals 1 and 7 were equivalent by trigonal domains or inversion symmetry except one peak. This observation could be linked to the varying observed structural factors presented in Figs. 7 and 11.

[1] N. A. Spaldin and R. Ramesh, Advances in magnetoelectric multiferroics, Nat. Mater. **18**, 203 (2019).

[2] M. Mostovoy, Advances in magnetoelectric multiferroics, npj Spintronics **2**, 18 (2024).

[3] S.-W. Cheong and M. Mostovoy, Multiferroics: A magnetic twist for ferroelectricity, Nat. Mater. **6**, 13 (2007).

[4] C. Gong, E. M. Kim, Y. Wang, G. Lee, and X. Zhang, Multiferroicity in atomic van der Waals heterostructures, Nat. Commun. **10**, 2657 (2019).

[5] R. Ramesh and N. A. Spaldin, Multiferroics: Progress and prospects in thin films, Nat. Mater. **6**, 21 (2007).

[6] Z. Wang, G. Xu, X. Jiang, L. Yang, Q. Gao, C. Li, D. Li, D. Liu, and B. Cui, 2D multiferroics in as-substituted bilayer α-In_2Se_3 with enhanced magnetic moments for next-generation nonvolatile memory device, Adv. Electron. Mater. **10**, 2300642 (2024).

[7] N. A. Hill, Why are there so few magnetic ferroelectrics? J. Phys. Chem. B **104**, 6694 (2000).

[8] J.-M. Hu, C.-G. Duan, C.-W. Nan, and L.-Q. Chen, Understanding and designing magnetoelectric heterostructures guided by computation: Progresses, remaining questions, and perspectives, npj Comput. Mater. **3**, 18 (2017).

[9] H. Palneedi, V. Annapureddy, S. Priya, and J. Ryu, Status and perspectives of multiferroic magnetoelectric composite materials and applications, Actuators **5**, 9 (2016).

[10] A. Hirohata, K. Yamada, Y. Nakatani, I.-L. Prejbeanu, B. Diény, P. Pirro, and B. Hillebrands, Review on spintronics: Principles and device applications, J. Magn. Magn. Mater. **509**, 166711 (2020).

[11] C. Lu, M. Wu, L. Lin, and J.-M. Liu, Single-phase multiferroics: New materials, phenomena, and physics, Natl. Sci. Rev. **6**, 653 (2019).

[12] S. Manipatruni, D. E. Nikonov, C.-C. Lin, T. A. Gosavi, H. Liu, B. Prasad, Y.-L. Huang, E. Bonturim, R. Ramesh, and I. A. Young, Scalable energy-efficient magnetoelectric spin–orbit logic, Nature (London) **565**, 35 (2019).

[13] E. F. Bertaut, L. Corliss, F. Forrat, R. Aleonard, and R. Pauthenet, Etude de niobates et tantalates de metaux de transition bivalents, J. Phys. Chem. Solids **21**, 234 (1961).

[14] Y. Fang, W. P. Zhou, S. M. Yan, R. Bai, Z. H. Qian, Q. Y. Xu, D. H. Wang, and Y. W. Du, Magnetic-field-induced dielectric anomaly and electric polarization in $Mn_4Nb_2O_9$, J. Appl. Phys. **117**, 17B712 (2015).

[15] S. N. Panja, P. Manuel, and S. Nair, Anisotropy in the magnetization and magnetoelectric response of single crystalline $Mn_4Ta_2O_9$, Phys. Rev. B **103**, 014422 (2021).

[16] J. H. Zhang, Y. S. Tang, L. Lin, L. Y. Li, G. Z. Zhou, B. Yang, L. Huang, X. Y. Li, G. Y. Li, S. H. Zheng, M. F. Liu, M. Zeng, D. Wu, Z. B. Yan, X. K. Huang, C. Chen, X. P. Jiang, and J.-M. Liu, Electric polarization reversal and nonlinear magnetoelectric coupling in the honeycomb antiferromagnet $Fe_4Nb_2O_9$ single crystal, Phys. Rev. B **107**, 024108 (2023).

[17] A. Maignan and C. Martin, $Fe_4Nb_2O_9$: A magnetoelectric antiferromagnet, Phys. Rev. B **97**, 161106 (2018).

[18] N. D. Khanh, N. Abe, S. Kimura, Y. Tokunaga, and T. Arima, Manipulation of electric polarization with rotating magnetic field in a honeycomb antiferromagnet $Co_4Nb_2O_9$, Phys. Rev. B **96**, 094434 (2017).

[19] N. Lee, D. G. Oh, S. Choi, J. Y. Moon, J. H. Kim, H. J. Shin, K. Son, J. Nuss, V. Kiryukhin, and Y. J. Choi, Highly nonlinear magnetoelectric effect in buckled-honeycomb antiferromagnetic $Co_4Ta_2O_9$, Sci. Rep. **10**, 12362 (2020).

[20] N. D. Khanh, N. Abe, H. Sagayama, A. Nakao, T. Hanashima, R. Kiyanagi, Y. Tokunaga, and T. Arima, Magnetoelectric coupling in the honeycomb antiferromagnet $Co_4Nb_2O_9$, Phys. Rev. B **93**, 075117 (2016).

[21] N. Narayanan, A. Senyshyn, D. Mikhailova, T. Faske, T. Lu, Z. Liu, B. Weise, H. Ehrenberg, R. A. Mole, W. D. Hutchison, H. Fuess, G. J. McIntyre, Y. Liu, and D. Yu, Magnetic structure and spin correlations in magnetoelectric honeycomb $Mn_4Ta_2O_9$, Phys. Rev. B **98**, 134438 (2018).

[22] R. Jana, D. Sheptyakov, X. Ma, J. A. Alonso, M. Pi, A. Muñoz, Z. Liu, L. Zhao, N. Su, S. Jin, X. Ma, K. Sun, D. Chen, S. Dong, Y. Chai, S. Li, and J. Cheng, Low-temperature crystal and magnetic structures of the magnetoelectric material $Fe_4Nb_2O_9$, Phys. Rev. B **100**, 094109 (2019).

[23] S. Choi, D. G. Oh, M. J. Gutmann, S. Pan, G. Kim, K. Son, J. Kim, N. Lee, S.-W. Cheong, Y. J. Choi, and V. Kiryukhin, Noncollinear antiferromagnetic order in the buckled honeycomb lattice of magnetoelectric $Co_4Ta_2O_9$ determined by single-crystal neutron diffraction, Phys. Rev. B **102**, 214404 (2020).

[24] G. Deng, G. Zhao, S. Zhu, Z. Feng, W. Ren, S. Cao, A. Studer, and G. J. McIntyre, Spin dynamics, critical scattering and magnetoelectric coupling mechanism of $Mn_4Nb_2O_9$, New J. Phys. **24**, 083007 (2022).

[25] A. Maignan and C. Martin, Enhancement of T_N induced by magnetic dilution in the linear magnetoelectric $Mn_4Nb_2O_9$, Appl. Phys. Lett. **124**, 162404 (2024).

[26] R. Datta, K. Kumar, D. G. Oh, D. Kim, R. Goel, N. Lee, A. Go, Y. J. Choi, V. Kiryukhin, and S. Choi, High-resolution neutron diffraction determination of noncollinear antiferromagnetic order in the honeycomb magnetoelectric $Fe_4Nb_2O_9$, Phys. Rev. B **112**, 134439 (2025).

[27] S. Mugiraneza and A. M. Hallas, Tutorial: A beginner's guide to interpreting magnetic susceptibility data with the Curie-Weiss law, Commun. Phys. **5**, 95 (2022).

[28] D. A. Keen, M. J. Gutmann, and C. C. Wilson, SXD—The single-crystal diffractometer at the ISIS spallation neutron source, J. Appl. Crystallogr. **39**, 714 (2006).

[29] V. Petříček, M. Dušek, and L. Palatinus, Crystallographic computing system JANA2006: General features, Z. Kristallogr. – Cryst. Mater. **229**, 345 (2014).

[30] P. J. Becker and P. Coppens, Extinction within the limit of validity of the Darwin transfer equations. II. Refinement of extinction in spherical crystals of SrF_2 and LiF, Acta Cryst. A **30**, 148 (1974).

[31] R. C. Clark and J. S. Reid, The analytical calculation of absorption in multifaceted crystals, Acta Cryst. A **51**, 887 (1995).

[32] M. Gutmann, SXD2001—A program for treating data from TOF neutron single-crystal diffraction, Acta Cryst. A **61**, c164 (2005).

[33] M. Aroyo, J. Perez-Mato, D. Orobengoa, E. Tasci, G. De La Flor, and A. Kirov, Crystallography online: Bilbao crystallographic server, Bulg. Chem. Commun. **43**, 183 (2011).

[34] I. E. Dzyaloshinskii, On the magneto-electrical effects in antiferromagnets, J. Exp. Theor. Phys. **10**, 628 (1960).

[35] C. Topping and S. Blundell, A.C. susceptibility as a probe of low-frequency magnetic dynamics, J. Phys.: Condens. Matter **31**, 013001 (2019).

[36] M. Bałanda, AC susceptibility studies of phase transitions and magnetic relaxation: Conventional, molecular and low-dimensional magnets, Acta Phys. Pol. A **124**, 964 (2013).

[37] A. A. Belik and E. Takayama-Muromachi, AC susceptibility studies of multiferroic $BiMnO_3$ and solid solutions between $BiMnO_3$ and $BiScO_3$, J. Phys.: Condens. Matter **20**, 025211 (2008).

[38] P. Yadav, S. Lee, G. L. Pascut, J. Kim, M. J. Gutmann, X. Xu, B. Gao, S.-W. Cheong, V. Kiryukhin, and S. Choi, Noncollinear magnetic order, in-plane anisotropy, and magnetoelectric coupling in the pyroelectric honeycomb antiferromagnet $Ni_2Mo_3O_8$, Phys. Rev. Res. **5**, 033099 (2023).

[39] C. A. M. Mulder, A. J. van Duyneveldt, and J. A. Mydosh, Susceptibility of the CuMn spin-glass: Frequency and field dependences, Phys. Rev. B **23**, 1384 (1981).

[40] M. Ceglarska, O. Stefańczyk, S.-i. Ohkoshi, and A. M. Majcher-Fitas, Influence of magnetic dilution on relaxation processes in a solid solution comprising tetrahedral Co/Zn II complexes, Dalton Trans. **49**, 6807 (2020).

[41] H. Katsura, N. Nagaosa, and A. V. Balatsky, Spin current and magnetoelectric effect in noncollinear magnets, Phys. Rev. Lett. **95**, 057205 (2005).

[42] I. A. Sergienko, C. Şen, and E. Dagotto, Ferroelectricity in the magnetic *e*-phase of orthorhombic perovskites, Phys. Rev. Lett. **97**, 227204 (2006).

[43] T.-H. Arima, Ferroelectricity induced by proper-screw type magnetic order, J. Phys. Soc. Jpn. **76**, 073702 (2007).

[44] S.-W. Cheong, SOS: Symmetry-operational similarity, npj Quantum Mater. **4**, 53 (2019).

[45] Y. Fang, Y. Q. Song, W. P. Zhou, R. Zhao, R. J. Tang, H. Yang, L. Y. Lv, S. G. Yang, D. H. Wang, and Y. W. Du, Large magnetoelectric coupling in $Co_4Nb_2O_9$, Sci. Rep. **4**, 3860 (2014).

[46] W. Liu, L. Li, L. Tao, Z. Liu, X. Wang, Y. Sui, and Y. Wang, Evidence of linear magnetoelectric effect in $Mn_4Nb_2O_9$ single crystal, J. Alloys Compd. **886**, 161272 (2021).

[47] I. Mazin, Editorial: Altermagnetism—A new punch line of fundamental magnetism, Phys. Rev. X **12**, 040002 (2022).

[48] S.-W. Cheong and F.-T. Huang, Altermagnetism with noncollinear spins, npj Quantum Mater. **9**, 13 (2024).

[49] S.-W. Cheong and F.-T. Huang, Altermagnetism classification, npj Quantum Mater. **10**, 38 (2025).

[50] S. Choi, V. Kiryukhin, and M. Gutmann, Reliable determination of noncollinear magnetic order of $Co_4Nb_2O_9$ to explain its nontrivial magnetoelectricity, STFC ISIS Neutron and Muon Source (2020), doi:10.5286/ISIS.E.RB2000175-1.

[51] D. Hüser, L. E. Wenger, A. J. van Duyneveldt, and J. A. Mydosh, Dynamical behavior of the susceptibility around the freezing temperature in (Eu,Sr)S, Phys. Rev. B **27**, 3100 (1983).